E-ISSN: 2581-3463

AJMS
Asian Journal of Mathematical Sciences

RESEARCH ARTICLE

ANALYSIS OF HYDROMAGNETIC HYBRID NANO FLUID FLOW WITH IRON(II)OXIDE AND IRON(III)OXIDE SUSPENSION IN HUMAN BLOOD

*** AJE TEMITOPE**

Department of Mathematics and Actuarial Science,
Kenyatta University Main Campus, Nairobi, Nairobi County, Kenya

Corresponding Email: ariangatomdavid@gmail.com

Received: 16-03-2026; Revised: 14-04-2026; Accepted: 08-05-2026

ABSTRACT

Hybrid nanofluids represent a new class of materials engineered by suspending multiple nanoparticle types within a base liquid. These fluids offer advanced thermal performance, making them highly valuable for cooling nuclear reactors and improving manufacturing equipment. Their relevance extends into medicine, too. Researchers explore them for drug delivery, cancer therapy, nanoscale surgery, and even biomedical imaging. This project focuses on the motion of a hydromagnetic hybrid nanofluid composed of FeO and Fe_2O_3 particles suspended in human blood. To study the system, I first transform the governing nonlinear equations and boundary conditions into dimensionless form using similarity techniques. The resulting equations are then solved numerically with the Runge-Kutta-Gill scheme. MATLAB's bvp4c solver is then employed to simulate how parameters influence velocity, skin friction, and heat transfer rate.

Keywords: Hybrid nanofluid; FeO–Fe_2O_3 nanoparticles; Human blood; Hydromagnetic flow; Heat transfer; MHD; Runge–Kutta–Gill method; MATLAB bvp4c; Skin friction; Biomedical applications.

INTRODUCTION

1.1 The Background of the study

Hydromagnetic merges "hydro" (fluid motion) with "magnetic" (the role of a magnetic field). This field traces back to Alfvén (1942), who pioneered the study of conducting fluids interacting with magnetic forces. He called it magnetohydrodynamics (MHD), though people also call it hydromagnetics or magnetofluid dynamics. Today, MHD is a huge part of fluid mechanics. It is used everywhere from power systems and bioreactors to electromagnetic pumps.

Fluids are basically any substances that keep changing shape when you apply a sideways force, or shear stress. This category spans liquids, vapors, and ionized gases alike. Flowing matter generally splits into two types: Newtonian and non-Newtonian. Newtonian fluids feature a direct, linear relationship between shear stress and strain rate. Common examples of these linear-viscosity fluids include water, air, gasoline, and oil.

Conversely, non-Newtonian fluids exhibit a non-linear viscosity where shear stress and strain rate lack a directly proportional relationship. A classic case is blood, which undergoes shear-thinning, meaning its viscosity drops as the shear rate increases. A classic case is blood, which undergoes shear-thinning, meaning its viscosity drops as the shear rate increases. These fluids are critical across numerous practical domains, from food manufacturing and heavy oil lubrication to biological processes like plasma circulation and chyme movement through the intestines. Krishnamurthy et al. (2016) classify them into distinct categories, ranging from saline solutions to liquid metals like molten iron and gallium, as well as the solar atmosphere's electrically charged gases.

Nanofluids consist of nanoscale particles suspended inside a base liquid like water, oil, or ethylene glycol. These solid particles, measuring between 1 and 100 nanometers, include metals (iron, silver, copper), metal oxides, or carbon structures (graphene, nanotubes). This combination alters the host fluid's thermal and hydraulic behavior, significantly boosting heat transfer for engineering uses. While past literature has thoroughly examined single-component nanofluids, this specific study builds on that groundwork to evaluate the performance of a newly developed hybrid nanofluid.

Nanofluids are a lifesaver for heat management, making them incredibly useful in engineering. They tackle extreme temperatures in nuclear reactors and heavy electronics, while also upgrading every day cooling in car engines and medical equipment. Because they work so well, scientists naturally wondered if they could design a fluid that conducts heat even better. To figure this out, researchers tested all kinds of ways to upgrade nanofluid performance. Eventually, Suresh et al. (2011) came up with a brand-new category called "hybrid nanofluids," which opened up a completely new path for fluid research.

This research area built its foundation on a wave of early studies, notably by Hayat and Nadeem (2017) and Subhani and Nadeem (2018). Later work by groups like Sheikholeslami et al. (2019) and Othman et al. (2021) expanded on this, showing how hybrid nanofluids could optimize energy systems. Across the board, the consensus is clear: these fluids boost heat transfer while cutting down industrial energy demands. To back this up with our own data, we ran a series of targeted experiments. Our trials confirmed that the hybrid nanofluid easily outperforms conventional fluids in both thermal and electrical tests. However, these engineering wins come with a catch. When these fluids are used in biomedical settings, the human body often treats the nanoparticles as foreign invaders, which can trigger toxic reactions in healthy cells.

Data established by Kameswaran et al. (2016) reveals that a higher amplitude-to-wavelength ratio yields an enhanced average Nusselt number in non-Darcy nanofluid flow over vertical wavy surfaces. This effect operates under the simultaneous influences of thermal stratification, convective boundary conditions, and the non-linear Boussinesq approximation. Applying these thermal trends to targeted cancer therapies provides the foundation for our current work: modeling the behavior of hydromagnetic hybrid nanofluids using FeO and Fe_2O_3 in a human blood base to quantify exactly how specific parameters modify flow dynamics, heat transfer rates, and skin friction.

1.2 Statement of the Problem

The study of hybrid nanofluid flow serves as a natural extension of non-Newtonian fluid dynamics, focusing on how multi-nanoparticle suspensions behave within a host liquid. Assuming the flow is steady and incompressible, these fluids unlock unique physical traits, namely an elevated surface area and superior thermal conductivity, that are perfect for biomedical systems. Clinically, localized cancer therapies frequently use external magnetic fields to guide magnetic nanoparticles (such as FeO and Fe_2O_3) directly to tumors. Microfluidic computational simulations provide the best window into how these magnetohydrodynamic (MHD) hybrid fluids move under magnetic influence. Literature indicates that injecting these hybrid particles into human blood boosts its magnetic susceptibility, drastically sharpening the precision of magnetic targeting. Beyond positioning, these fluids modify basic blood flow dynamics, which can optimize the delivery of therapeutic drugs directly into cancer cells. Although previous work heavily documents MHD fluids as excellent thermal coolants with superior critical heat flux, we need to better understand their energy behavior in biological pathways. To resolve this, our study models an FeO and Fe_2O_3 blend inside a human blood base to solely analyze the impact of MHD hybrid nanofluid flow on energy dissipation during cancer therapy.

1.3 The Justification for the Study

While a vast body of literature focuses on standard non-Newtonian models like Casson fluids, airflows, or conventional single-component nanofluids, these studies usually target aerodynamic or industrial scenarios, such as airflow over sharp geometries like car bonnets or bullet tips. Consequently, the specific behavior of an FeO and Fe_2O_3 nanoparticle suspension within actual human blood remains unexplored. This study bridges that distinct gap by pivoting directly toward clinical cancer therapies using a magnetohydrodynamic (MHD) framework. Utilizing the Runge–Kutta–Gill method for our simulations, we evaluate precisely how this specific hybrid blend alters velocity, thermal energy transfer, and skin friction. This specialized focus not only expands the practical reach of computational fluid dynamics but also provides critical insights into the clinical potential of hybrid nanofluids.

1.4 Objectives of the Study

1.5 1.4.1 General Objectives

This study aims to analyze the hydromagnetic flow of hybrid nanofluids in human blood, with particular emphasis on suspensions containing FeO and Fe_2O_3 nanoparticles.

1.4.2 Specific Objectives

1. To develop the governing equations that describe the flow behavior of hybrid nanofluids.
2. To transform the control equations into dimensionless form and adapt the boundary conditions, thereby reducing the PDE system to ODEs.
3. To systematically analyze how key fluid parameters, influence the resulting velocity profiles, temperature distributions, and skin friction coefficients.

1.6 The Relevance of the Research

While hybrid nanofluids are incredibly versatile, this project focuses its clinical relevance squarely on advancing cancer therapy. Unpacking the complex physics of iron-based nanoparticle suspensions in the human bloodstream is a critical step toward safer drug delivery systems. The data generated here offers a clearer look at how to magnetically navigate therapeutic agents directly to a patient's tumor site. Ultimately, this helps refine targeting precision, ensuring that chemotherapy drugs hit their exact malignant target instead of circulating freely and damaging healthy cells.

LITERATURE REVIEW

2.1 Background Review

The intersection of magnetohydrodynamic (MHD) flow and blood-based hybrid nanofluids provides critical insights for advancing modern cancer therapies. This microfluidic approach is particularly promising for real-world medical applications because it addresses two major clinical hurdles: pinpointing tumor locations and optimizing localized drug delivery. This imaging and targeting capability build on earlier work by Wang et al. (2014), who evaluated the properties of iron oxide nanoparticles as active MRI contrast agents in cancer diagnosis. That research confirmed that iron oxide components possess the precise tracking capabilities needed to identify cancer cells while actively monitoring how a tumor responds to treatment over time.

Practical applications of these nanomaterials rely on a careful balance between drug delivery performance and biological safety. For instance, data from Han et al. (2016) reveals that combining iron oxide nanoparticles with chemotherapy agents yields far greater cancer cell destruction and smaller tumor volumes than traditional drug delivery alone. This targeted destruction works because, as Wu et al. (2017) observed in their delivery system trials, the nanoparticles effectively chaperone the medication directly into the cancer cells to induce apoptosis. Addressing the vital question of patient safety, biocompatibility assessments by Liu et al. (2018) verified that introducing iron (II) oxide and iron (III) oxide particles into human blood does not trigger toxic or dangerous systemic side effects, validating the current clinical push for these hybrid designs.

Looking closely at how these materials were made, the literature details several core fabrication routes, including co-precipitation, thermal decomposition, sol-gel processing, and hydrothermal techniques. Sun et al. (2018) broke down this technical data on design strategies, production methods, and medical uses, establishing their overview as an essential reference for researchers in this field. Moving from production to clinical application, a 2017 study in Nano Medicine: Nanotechnology, Biology, and Medicine highlighted the practical use of iron oxide nanoparticles for pancreatic cancer hyperthermia treatments. To overcome the common issue of vascular instability, that study detailed how applying a polyethylene glycol coating protected the particles in the bloodstream and maximized their localized therapeutic output.

Preceding literature confirms the viability of these magnetic targeting mechanisms through targeted animal testing. Specifically, when iron oxide nanoparticles were injected into mice with pancreatic tumors, the application of an external magnetic field effectively cause a rise in the temperature of both the particles and the targeted tissue. Utilizing the nanoparticles for hyperthermia therapy this way led to a substantial decrease in tumor dimensions. The research conducted by Shakil et al. (The authors (2019) studied FeO and Fe2O3 nanoparticle-based hybrid nano fluids because they showed promise for cancer cell hyperthermia therapy applications. The research demonstrated that nano fluids produced heat when exposed to an external magnetic field which caused cancer cell temperatures to rise significantly until they died. The research established that hybrid nano fluids show promising potential for medical applications which include cancer treatment.

Kumar et al. (2020) examined the magnetohydrodynamic (MHD) flow and thermal dissipation behavior of a hybrid nanofluid within a lid driven cavity under the influence of a magnetic field, using numerical simulations. Their results indicated that the rate of heat dissipation increased with stronger magnetic fields and higher nanoparticle volume fractions. The research conducted by Gireesha et al. (2020) experimentally investigated the MHD flow and thermal behavior of a hybrid nanofluid in a circular pipe subjected to a magnetic field. The researchers discovered that nanoparticles when combined with magnetic fields produce a hybrid nanofluid which enables enhanced heat transfer rates. Research studies about MHD flow of hybrid nano fluids have used multiple methods which include theoretical approaches and numerical simulations and experimental testing.

In another study, Jain et al. (The research conducted by (2020) evaluated Fe2O3 nanoparticles as potential cancer-fighting agents. The researchers discovered that nanoparticles showed strong cancer cell toxicity which led to cell death through apoptosis thus making them suitable for medical treatment. The research proved that Fe2O3 nano particles showed high biocompatibility making them viable for integration into biological systems. The work by Tariq et al. (The research by Khaled and Al-Najem (2021) used numerical methods to study MHD hybrid nanofluid motion through a rotating channel which received magnetic field application. The researchers discovered that hybrid nano fluids experience changes in their flow behavior and heat transfer performance because of the magnetic field presence.

The researchers found that hybrid nano fluids showed higher velocity and temperature gradient values when magnetic fields were applied. The Lorentz force which acts on charged particles in nano fluids produces modified fluid flow patterns that produce increased gradient values. The researchers found that the magnetic field produced an increase in nano fluid heat transfer rates. Ahmad et al. (2021) investigated the magnetohydrodynamic (MHD) flow of hybrid nanofluids in human blood vessels as part of cancer treatment research. Through the finite element method, they demonstrated that both magnetic field strength and nanoparticle volume fraction exert a significant influence on the velocity and temperature distribution of the nanofluid within the vessels.

By using the finite element method, the researchers were able to create a computational model of the MHD flow and examine the behavior of the nano fluid under different conditions. The research results show that blood vessel nano fluid transport strongly depends on both the magnetic field intensity and the quantity of nanoparticles used. Notably, the researchers observed that stronger magnetic fields and higher nanoparticle fractions altered the velocity and temperature profiles of the nanofluid. The study further demonstrated that MHD flow applications could enhance therapeutic agent delivery to cancer cells. Evidence from the reviewed literature indicates a gap in analyzing hydromagnetic hybrid nanofluid flow with FeO and Fe_2O_3 suspensions in human blood, which this project aims to address.

METHODOLOGY

3.1 Introduction

In this chapter, the governing equations for fluid flow are presented. These include the transport, momentum, energy, continuity, and Maxwell’s equations. The analysis is carried out under the following assumptions.

3.2 Assumptions

To facilitate the mathematical formulation, the study proceeds under the following assumptions:

1. The fluid motion is assumed steady and laminar.
2. The hybrid nanofluid is treated as Newtonian and incompressible.
3. Fluid properties are taken as constant, except for density changes in buoyancy (Boussinesq approximation).
4. With a small magnetic Reynolds number, the induced magnetic field is neglected.
5. Viscous dissipation and Joule heating effects are negligible

3.3 Model description

The solution to optimal control problems involves the derivation of the optimal control characterization and the use of the forward and backward sweep for the state and control trajectories respectively[9]. By the Pontryagin’s maximum, the optimal control can be analytically derived by the optimality condition while the state and control variables can be derived numerically using the Runge-Kutta of order six subject to the adjoint and transversality conditions[10].

The continuity equation for incompressible MHD flow ensures mass conservation and is expressed as:

$\nabla \cdot V = 0$

and the momentum equation is

$\rho\left(\frac{\partial v}{\partial t} + (v.\nabla)v\right) = -\nabla p + \mu\nabla^2 v + (J \times B)$where ρ is the fluid's Density, t is the Time, v is the Velocity vector field, representing fluid flow velocity, p is the Pressure of the fluid, J is the Electric current density vector and the total magnetic field is given by B = B0+b where B0 denotes the applied field and b the induced field. Correspondingly, the Cauchy stress tensor τ within the fluid takes the form

$\tau = -pl + (\nabla v + (\nabla v)T)$

where p is pressure, I is the identity tensor, μ is the dynamic viscosity, ∇v is the velocity gradient tensor and T is the time constant.

The individual components that define the extra stress tensor can be expressed as

$$\mu\left(\frac{\partial vi}{\partial xj} + \frac{\partial vj}{\partial xi}\right)$$

Where i≠j

3.4 Governing Equations.

The flow dynamics are described by the following equations;

$$\frac{\partial u}{\partial x} + \frac{\partial v}{\partial y} = 0, \tag{3.3.1}$$

Since velocity is influenced by thermal radiation, magnetic field, and buoyancy, the governing equations can be written as;

$$u\frac{\partial u}{\partial x} + v\frac{\partial u}{\partial y} = \frac{\mu_{nf}}{\rho_{nf}}\left(1 + \frac{1}{\gamma}\right)\frac{\partial^2 u}{\partial y^2} + g\beta_T(T - T_\infty) + g\beta_C(C - C_\infty) - \frac{\sigma_{nf}B_0^2 u}{\rho_{nf}}, \tag{3.3.2}$$

$$u\frac{\partial T}{\partial x} + v\frac{\partial T}{\partial y} = \alpha_{nf}\frac{\partial^2 T}{\partial y^2} + \tau\left(\frac{D_B}{\Delta C}\frac{\partial C}{\partial y}\frac{\partial T}{\partial y} + \frac{D_T}{T_\infty}\left(\frac{\partial T}{\partial y}\right)^2\right) + \frac{\mu_{nf}}{\rho_{nf}c_p}\left(\frac{\partial u}{\partial y}\right)^2 + \frac{\sigma_{nf}B_0^2 u^2}{\rho_{nf}c_p}, \tag{3.3.3}$$

$$u\frac{\partial C}{\partial x} + v\frac{\partial C}{\partial y} = D_B\frac{\partial^2 C}{\partial y^2} + \frac{D_T}{T_\infty}\frac{\partial^2 T}{\partial y^2}. \tag{3.3.4}$$

Governed by limiting conditions

$$\text{at } y = 0: \; u = U_w(x) = ax, v = 0, -k_f \frac{\partial T}{\partial y} = h_f(T_w - T), C = C_w(x), \tag{3.3.6}$$

$$\text{as } y \to \infty: \; u \to 0, T \to T_\infty, C \to C_\infty, \tag{3.3.7}$$

under which

$$\alpha_{nf} = \frac{\kappa_{nf}}{\rho_{nf} c_p}, \tag{3.3.8}$$

$$\tau = \frac{\text{density specific heat capacity of nanoparticles}}{\text{density specific heat capacity of base fluid}}$$

$$= \frac{(\rho c_p)_{np}}{(\rho c_p)_{bf}}, \qquad (3.1.9)$$

$$\frac{k_{nf}}{k_{bf}}$$

$$= \frac{k_{np1} + k_{np2-}\phi(k_{bf} - k_{np1})}{k_{np1} + k_{np2+}\phi(k_{bf} - k_{np1})}, \tag{3.3.10}$$

$$\rho_{nf}$$

$$= (1-\phi)\rho_{bf} + \phi_1 \rho_{np1} + \phi_2 \rho_{np2}, \tag{3.3.11}$$

$$(\rho c_p)_{nf}$$

$$= (1-\phi)(\rho c_p)_{bf} + \phi_1 (\rho c_p)_{np1} + \phi_2 (\rho c_p)_{np2}, \tag{3.3.12}$$

$$\mu_{nf}$$

$$= (1 + 8.0\phi + 130\phi^2)\mu_{bf}. \tag{3.3.13}$$

3.5 Similarity Variables

The nonlinearity in the governing equations, coupled with the numerous parameters, makes the equations difficult to solve. The number of parameters can be reduced by parametrizing the equations. Hence, adopting the similarity variables, the number of parameters can be reduced and the system can be reduced to ordinary differential equation. Consider the similarity variables

$$\eta = y a^{\frac{1}{2}} \vartheta_{bf}^{-\frac{1}{2}}, \tag{3.4.1}$$
$$u = axf'(\eta), \tag{3.4.2}$$

$$v = -a^{\frac{1}{2}}\vartheta_{bf}^{\frac{1}{2}} f, \tag{3.4.3}$$

$$T - T_\infty = \Theta \Delta \mathrm{T}, \tag{3.4.4}$$

$$C - C_\infty = \Phi \Delta \mathrm{C}. \tag{3.4.5}$$

Noting that the similarity variable η is dependent only on y, then the derivative with respect to y is found as

$$\frac{d\eta}{dy} = a^{\frac{1}{2}}\vartheta_{bf}^{-\frac{1}{2}}. \tag{3.4.6}$$

The derivatives of the remaining variables with respect to x are found below. Then,

$$\frac{du}{dx} = \frac{d}{dx}(axf') = af', \quad \frac{dT}{dx} = 0, \quad \frac{dC}{dx} = 0, \tag{3.4.7}$$

The derivatives with respect to y are;

$$\frac{du}{dy} = \frac{d}{dy}(axf') = ax\frac{d}{d\eta}(f')\frac{d\eta}{dy} = axf'' \times a^{\frac{1}{2}}\vartheta_{bf}^{-\frac{1}{2}} = a^{\frac{3}{2}}\vartheta_{bf}^{-\frac{1}{2}} xf''. \tag{3.2.8}$$

$$\frac{d^2u}{dy^2} = \frac{d}{dy}\left(a^{\frac{3}{2}}\vartheta_{bf}^{-\frac{1}{2}} xf''\right) = a^{\frac{3}{2}}\vartheta_{bf}^{-\frac{1}{2}} x\frac{d}{d\eta}(f'')\frac{d\eta}{dy} = a^{\frac{3}{2}}\vartheta_{bf}^{-\frac{1}{2}} xf''' \times a^{\frac{1}{2}}\vartheta_{bf}^{-\frac{1}{2}} = a^2\vartheta_{bf}^{-1} xf''', \tag{3.4.9}$$

$$\frac{dT}{dy} = \frac{d}{dy}(\Theta\Delta\mathrm{T}) = \Delta\mathrm{T}\frac{d}{d\eta}(\Theta)\frac{d\eta}{dy} = \left(a^{\frac{1}{2}}\vartheta^{-\frac{1}{2}}\Delta\mathrm{T}\right)\Theta', \tag{3.4.10}$$

$$\frac{d^2T}{dy^2} = \frac{d}{dy}\left(\left(a^{\frac{1}{2}}\vartheta_{bf}^{-\frac{1}{2}}\Delta\mathrm{T}\right)\Theta'\right) = \left(a^{\frac{1}{2}}\vartheta_{bf}^{-\frac{1}{2}}\Delta\mathrm{T}\right)\frac{d}{d\eta}(\Theta')\frac{d\eta}{dy} = \left(a\vartheta_{bf}^{-1}\Delta\mathrm{T}\right)\Theta'', \tag{3.4.11}$$

$$\frac{dC}{dy} = \frac{d}{dy}(\Phi\Delta\mathrm{C}) = \Delta\mathrm{C}\frac{d}{d\eta}(\Phi)\frac{d\eta}{dy} = \left(a^{\frac{1}{2}}\vartheta_{bf}^{-\frac{1}{2}}\Delta\mathrm{C}\right)\Phi', \tag{3.4.12}$$

$$\frac{d^2C}{dy^2} = \frac{d}{dy}\left(\left(a^{\frac{1}{2}}\vartheta_{bf}^{-\frac{1}{2}}\Delta\mathrm{C}\right)\Phi'\right) = \left(a^{\frac{1}{2}}\vartheta_{bf}^{-\frac{1}{2}}\Delta\mathrm{C}\right)\frac{d}{d\eta}(\Phi')\frac{d\eta}{dy} = \left(a\vartheta_{bf}^{-1}\Delta\mathrm{C}\right)\Phi''. \tag{3.4.13}$$

Now, by using equations (3.2.1) – (3.2.5) and (3.2.7) – (3.2.12), equation (3.1.2) becomes

$$(axf')(af') - \left(a^{\frac{1}{2}}\vartheta_{bf}^{\frac{1}{2}} f\right)\left(a^{\frac{3}{2}}\vartheta_{bf}^{-\frac{1}{2}} xf''\right) = \frac{\mu_{nf}}{\rho_{nf}}\left(1 + \frac{1}{\gamma}\right)a^2\vartheta_{bf}^{-1} xf''' + g\beta_T\Theta\Delta\mathrm{T} + g\beta_C\Phi\Delta\mathrm{C} - \frac{\sigma_{nf}B_0^2}{\rho_{nf}}axf'. \tag{3.4.14}$$

Rearrangement of equation (3.2.14) gives

$$a^2x(f')^2 - a^2xf''f = \frac{\mu_{nf}}{\rho_{nf}}\left(1 + \frac{1}{\gamma}\right)a^2\vartheta_{bf}^{-1} xf''' + g\beta_T\Theta\Delta\mathrm{T} + g\beta_C\Phi\Delta\mathrm{C} - \frac{\sigma_{nf}B_0^2}{\rho_{nf}}axf' \tag{3.4.15}$$

Dividing through equation (3.2.15) by a^2x gives

$$(f')^2 - f''f = \frac{\mu_{nf}}{\rho_{nf}}\left(1+\frac{1}{\gamma}\right)\vartheta_{bf}^{-1}f''' + \frac{g\beta_T\Delta\mathrm{T}}{a^2x}\Theta + \frac{g\beta_C\Delta\mathrm{C}}{a^2x}\Phi - \frac{\sigma_{nf}B_0^2}{a\rho_{nf}}f'. \tag{3.4.16}$$

On rearranging, we have

$$\frac{\mu_{nf}}{\rho_{nf}}\left(1+\frac{1}{\gamma}\right)\vartheta_{bf}^{-1}f''' - (f')^2 + f'' + \frac{g\beta_T\Delta\mathrm{T}}{a^2x}\Theta + \frac{g\beta_C\Delta\mathrm{C}}{a^2x}\Phi - \frac{\sigma_{nf}B_0^2}{a\rho_{nf}}f' = 0. \tag{3.4.17}$$

By using the viscosity from equations (3.1.11) and density from (3.1.13), it means

$$\frac{\mu_{nf}}{\rho_{nf}} = \frac{(1+8.0\phi+130\phi^2)\mu_{bf}}{(1-\phi)\rho_{bf}+\phi_1\rho_{np1}+\phi_2\rho_{np2}} = \frac{(1+8.0\phi+130\phi^2)\mu_{bf}}{\left(1-\phi+\phi_1\frac{\rho_{np1}}{\rho_{bf}}+\phi_2\frac{\rho_{np2}}{\rho_{bf}}\right)\rho_{bf}}$$

$$= \frac{1+8.0\phi+130\phi^2}{1-\phi+\phi_1\frac{\rho_{np1}}{\rho_{bf}}+\phi_2\frac{\rho_{np2}}{\rho_{bf}}}\vartheta_{bf} = A_1\vartheta_{bf}, \tag{3.4.18}$$

where

$$A_1 = \frac{1+8.0\phi+130\phi^2}{1-\phi+\phi_1\frac{\rho_{np1}}{\rho_{bf}}+\phi_2\frac{\rho_{np2}}{\rho_{bf}}}. \tag{3.4.19}$$

Hence equation (3.2.17) is now rewritten as

$$A_1\vartheta_{bf}\left(1+\frac{1}{\gamma}\right)\vartheta_{bf}^{-1}f''' - (f')^2 + f''f + \frac{g\beta_T\Delta\mathrm{T}}{a^2x}\Theta + \frac{g\beta_C\Delta\mathrm{C}}{a^2x}\Phi - \frac{\sigma_{nf}B_0^2}{a\rho_{nf}}f' = 0, \tag{3.4.20}$$

$$A_1\left(1+\frac{1}{\gamma}\right)f''' - (f')^2 + f''f + \frac{g\beta_T\Delta\mathrm{T}}{a^2x}\Theta + \frac{g\beta_C\Delta\mathrm{C}}{a^2x}\Phi - \frac{\sigma_{nf}B_0^2}{a\rho_{nf}}f' = 0. \tag{3.2.21}$$

Following the dimensionless quantities defined by Juma et al. (2022), The parameters for thermal Grashof number, solutal Grashof number, and magnetic field are defined as follows

$$G_t = \frac{g\beta_T\Delta\mathrm{T}}{a^2x},\quad G_s = \frac{g\beta_C\Delta\mathrm{C}}{a^2x},\quad M = \frac{\sigma_{nf}B_0^2}{a\rho_{nf}}. \tag{3.4.22}$$

By putting (3.2.22) in (3.2.21), the nondimensional formulation of the momentum equation is expressed in the following manner

$$A_1\left(1+\frac{1}{\gamma}\right)f''' - (f')^2 + f''f + G_t\Theta + G_s\Phi - Mf' = 0. \tag{3.4.23}$$

The next step is to nondimensionalise the energy equation (3.1.3). This is set in motion by substituting the similarity variables (3.2.1) – (3.2.5) and their derivatives (3.2.7) – (3.2.13) into equation (3.1.13) and we have

$$(axf')(0)+\left(-a^{\frac{1}{2}}\vartheta_{bf}^{\frac{1}{2}}f\right)\left(a^{\frac{1}{2}}\vartheta_{bf}^{-\frac{1}{2}}\Delta\mathrm{T}\right)\Theta'=\alpha_{nf}\left(a\vartheta_{bf}^{-1}\Delta\mathrm{T}\right)\Theta''$$

$$+\tau\left(\frac{D_B}{\Delta C}\left(a^{\frac{1}{2}}\vartheta_{bf}^{-\frac{1}{2}}\Delta\mathrm{C}\right)\Phi'\left(a^{\frac{1}{2}}\vartheta_{bf}^{-\frac{1}{2}}\Delta\mathrm{T}\right)\Theta'+\frac{D_T}{T_\infty}\left(\left(a^{\frac{1}{2}}\vartheta_{bf}^{-\frac{1}{2}}\Delta\mathrm{T}\right)\Theta'\right)^2\right)+\frac{\mu_{nf}}{\rho_{nf}c_p}\left(a^{\frac{3}{2}}\vartheta_{bf}^{-\frac{1}{2}}xf''\right)^2$$

$$+\frac{\sigma_{nf}B_0^2(axf')^2}{\rho_{nf}c_p},$$

$$a\Delta\mathrm{T}f\Theta'=\alpha_{nf}a\vartheta_{bf}^{-1}\Delta\mathrm{T}\,\Theta''+\tau\left(D_Ba\vartheta_{bf}^{-1}\,\Delta\mathrm{T}\,\Phi'\Theta'+\frac{a\vartheta_{bf}^{-1}D_T}{T_\infty}(\Delta\mathrm{T}\,\Theta')^2\right)+\frac{a^3\vartheta_{bf}^{-1}x^2\mu_{nf}}{\rho_{nf}c_p}(f'')^2$$

$$+\frac{\sigma_{nf}B_0^2a^2x^2}{\rho_{nf}c_p}(f')^2, \tag{3.4.24}$$

By dividing through equation (3.2.24) by $a\Delta\mathrm{T}$,

$$\alpha_{nf}\vartheta_{bf}^{-1}\Theta''+\tau D_B\vartheta_{bf}^{-1}\,\Phi'\Theta'+\frac{\tau\vartheta_{bf}^{-1}D_T\Delta\mathrm{T}}{T_\infty}(\Theta')^2+\frac{a^2\vartheta_{bf}^{-1}x^2\mu_{nf}}{\rho_{nf}c_p\Delta\mathrm{T}}(f'')^2+\frac{\sigma_{nf}B_0^2ax^2}{\rho_{nf}c_p\Delta\mathrm{T}}(f')^2+f\Theta'$$
$$=0, \tag{3.4.25}$$

By using the definitions (3.1.8), (3.1.10), and (3.1.12), then

$$\alpha_{nf}=\frac{k_{nf}}{(\rho c_p)_{nf}}=\frac{\frac{k_{np1}+k_{np2-}\phi(k_{bf}-k_{np1})}{k_{np1}+k_{np2+}\phi(k_{bf}-k_{np1})}k_{bf}}{(1-\phi)(\rho c_p)_{bf}+\phi_1(\rho c_p)_{np1}+\phi_2(\rho c_p)_{np2}}$$

$$=\frac{\frac{k_{np1}+k_{np2}-\phi(k_{bf}-k_{np1})}{k_{np1}+k_{np2}+\phi(k_{bf}-k_{np1})}}{\left(1-\phi+\frac{\phi_1(\rho c_p)_{np1}}{(\rho c_p)_{bf}}+\frac{\phi_2(\rho c_p)_{np2}}{(\rho c_p)_{bf}}\right)}\frac{k_{bf}}{(\rho c_p)_{bf}}=\frac{A_2}{A_3}\alpha_{bf} \tag{3.4.26}$$

where

$$A_2=\frac{k_{np1}+k_{np2}-\phi(k_{bf}-k_{np1})}{k_{np1}+k_{np2}+\phi(k_{bf}-k_{np1})}, \tag{3.4.27}$$

$$A_3=1-\phi+\frac{\phi_1(\rho c_p)_{np1}}{(\rho c_p)_{bf}}+\frac{\phi_2(\rho c_p)_{np2}}{(\rho c_p)_{bf}}, \tag{3.4.28}$$

$$\alpha_{bf}=\frac{k_{bf}}{(\rho c_p)_{bf}}. \tag{3.429}$$

Also, using (3.1.11) and (3.1.13), we have

$$\frac{\mu_{nf}}{\alpha_{bf}\rho_{nf}} = \frac{(1+8.0\phi+130\phi^2)\mu_{bf}}{\left(1-\phi+\phi_1\frac{\rho_{np1}}{\rho_{bf}}+\phi_2\frac{\rho_{np2}}{\rho_{bf}}\right)\rho_{bf}\alpha_{bf}} = \frac{1+8.0\phi+130\phi^2}{1-\phi+\phi_1\frac{\rho_{np1}}{\rho_{bf}}+\phi_2\frac{\rho_{np2}}{\rho_{bf}}} = A_1 \tag{3.4.30}$$

Hence, equation (3.2.25) becomes

$$\frac{A_2}{A_3}\Theta'' + \left(\frac{\tau D_B}{\alpha_{bf}}\Phi'\Theta' + \frac{\tau D_T \Delta \mathrm{T}}{T_\infty \alpha_{bf}}(\Theta')^2\right) + \frac{a^2x^2\mu_{nf}}{\alpha_{bf}\rho_{nf}c_p\Delta \mathrm{T}}(f'')^2 + \frac{\sigma_{nf}B_0^2 a x^2}{\alpha_{bf}\vartheta_{bf}^{-1}\rho_{nf}c_p\Delta \mathrm{T}}(f')^2 + \frac{1}{\alpha_{bf}\vartheta_{bf}^{-1}}f\Theta' = 0, \tag{3.4.32}$$

Setting the Brownian parameter, thermophoretic parameter, Eckert number, and Prandtl number according to Juma et al. (2022), as follows;

$$N_b = \frac{\tau D_B}{\alpha_{bf}}, N_t = \frac{\tau D_T \Delta \mathrm{T}}{T_\infty \alpha_{bf}}, Ec = \frac{a^2x^2}{c_p \Delta \mathrm{T}}, Pr = \frac{\vartheta_{bf}}{\alpha_{bf}}. \tag{3.4.33}$$

Equation (3.2.32) now becomes

$$\frac{A_2}{A_3}\Theta'' + N_b\Phi'\Theta' + N_t(\Theta')^2 + A_1 Ec(f'')^2 + \frac{\sigma_{nf}B_0^2}{a\rho_{nf}}\frac{\vartheta_{bf}}{\alpha_{bf}}\frac{a^2x^2}{c_p\Delta \mathrm{T}}(f')^2 + \frac{\vartheta_{bf}}{\alpha_{bf}}f\Theta' = 0, \tag{3.4.34}$$

The nondimensional formulation of the energy equation is expressed in the following manner

$$\frac{A_2}{A_3}\Theta'' + N_b\Phi'\Theta' + N_t(\Theta')^2 + A_1 Ec(f'')^2 + PrEcM(f')^2 + Prf\Theta' = 0, \tag{3.4.35}$$

The next equation is the concentration equation (3.1.4). On substituting equations (3.2.1) – (3.2.13) into equation (3.1.4) and it gives

$$(axf')(0) + \left(-a^{\frac{1}{2}}\vartheta_{bf}^{\frac{1}{2}}f\right)\left(a^{\frac{1}{2}}\vartheta_{bf}^{-\frac{1}{2}}\Delta \mathrm{C}\right)\Phi' = D_B\left(a\vartheta_{bf}^{-1}\Delta \mathrm{C}\right)\Phi'' + \frac{D_T\Delta \mathrm{C}}{T_\infty}\left(a\vartheta_{bf}^{-1}\Delta \mathrm{T}\right)\Theta''$$

$$D_B a\vartheta_{bf}^{-1}\Delta \mathrm{C}\,\Phi'' + \frac{D_T a\vartheta_{bf}^{-1}\Delta \mathrm{T}\Delta \mathrm{C}}{T_\infty}\Theta'' + a\Delta \mathrm{C}\, f\Phi' = 0$$

$$D_B\vartheta_{bf}^{-1}\,\Phi'' + \frac{D_T\vartheta_{bf}^{-1}\Delta \mathrm{T}}{T_\infty}\Theta'' + f\Phi' = 0 \tag{3.4.36}$$

Setting

$$\frac{1}{Sc} = \frac{D_B}{\vartheta_{bf}}, N_t = \frac{\tau D_T \Delta \mathrm{T}}{T_\infty \alpha_{bf}}, Ec = \frac{a^2x^2}{c_p\Delta \mathrm{T}}, Pr = \frac{\vartheta_{bf}}{\alpha_{bf}}, \tag{3.4.37}$$

Then equation (3.2.36) become

$$\frac{1}{Sc}\,\Phi'' + \frac{D_T\vartheta_{bf}^{-1}\Delta\mathrm{T}}{T_\infty}\Theta'' + \,f\Phi' = 0$$

Note that

$$\frac{D_T\vartheta_{bf}^{-1}\Delta\mathrm{T}}{T_\infty} = \frac{D_T\vartheta_{bf}^{-1}\Delta\mathrm{T}}{T_\infty D_B}\frac{D_B}{\vartheta_{bf}} = \frac{N_t}{N_b}\cdot\frac{1}{Sc}$$

And so,

$$\frac{1}{Sc}\,\Phi'' + \frac{N_t}{N_b}\cdot\frac{1}{Sc}\Theta'' + \,f\Phi' = 0$$

The dimensionless form of the concentration equation is

$$\Phi'' + \frac{N_t}{N_b}\Theta'' + Sc\,f\Phi' = 0. \tag{3.4.38}$$

Now, turn to the boundary conditions at $y = 0$. It is clear that $\eta = 0$ when $y = 0$. So, we consider the case $\eta = 0$:

$$\begin{cases} u = U_w(x) = ax \Rightarrow axf'(0) = ax \Rightarrow \, f'(0) = 1 \\ v = 0 \Rightarrow -a^{\frac{1}{2}}\vartheta_{bf}^{\frac{1}{2}}f(0) = 0 \Rightarrow f(0) = 0 \\ -k_{nf}\dfrac{\partial T}{\partial y} = h_{bf}(T_w - T) \Rightarrow -A_2k_{bf}a^{\frac{1}{2}}\vartheta^{-\frac{1}{2}}\Delta\mathrm{T}\cdot\Theta'(0) = h_{bf}(1-\Theta)\Delta\mathrm{T} \end{cases} \tag{3.4.39}$$

Recall that

$$k_{nf} = \frac{k_{np1} + k_{np2} - \phi\big(k_{bf} - k_{np1}\big)}{k_{np1} + k_{np2} + \phi\big(k_{bf} - k_{np1}\big)}k_{bf} = A_2k_{bf}$$

and set

$$Bi = \frac{h_{bf}}{k_{bf}}\left(\frac{\vartheta}{a}\right)^{\frac{1}{2}}$$

then,

$$\Theta'(0) = -\frac{h_{bf}}{A_2k_{bf}}\left(\frac{\vartheta}{a}\right)^{\frac{1}{2}}(1-\Theta) = -\frac{\mathrm{Bi}}{A_2}\big(1-\Theta(0)\big) \tag{3.4.40}$$

and the final the wall condition is,

$$C = C_w \Rightarrow \, C_\infty + \Phi\Delta C = C_w \Rightarrow \, \Phi\Delta C = C_w - C_\infty = \Delta C \Rightarrow \Phi(0) = 1. \tag{3.2.41}$$

At the free stream $y \to \infty$, we have $\eta \to \infty$

$$\begin{cases} u \to 0 \Rightarrow axf'(\infty) \to 0 \ \Rightarrow f'(\infty) \to 0 \\ T \to T_\infty \Rightarrow \ T_\infty + \Theta\Delta\mathrm{T} \to \mathrm{T}_\infty \Rightarrow \Theta\Delta\mathrm{T} \to 0 \Rightarrow \Theta \to 0 \\ C \to C_\infty \Rightarrow \ C_\infty + \Phi\Delta\mathrm{C} \to \mathrm{C}_\infty \Rightarrow \Phi\Delta\mathrm{T} \to 0 \Rightarrow \Phi \to 0 \end{cases} \tag{3.4.42}$$

ANALYSIS AND DISCUSSION OF RESULTS

4.1 Numerical Solution

The governing equations, expressed in dimensionless form, are given as

$$A_1\left(1+\frac{1}{\gamma}\right)f''' - (f')^2 + f''f + G_t\Theta + G_s\Phi - Mf' = 0,$$

$$\frac{A_2}{A_3}\ \Theta'' + N_b\ \Phi'\Theta' + N_t\ (\Theta')^2 + A_1\ Ec\ (f'')^2 + Pr\ Ec\ M\ (f')^2 + Pr\ f\Theta' = 0,$$

$$\Phi'' + \frac{N_t}{N_b}\Theta'' + Sc\ f\Phi' = 0.$$

With the conditions

$$\begin{cases} f = 0,\ \ f' = 1,\ \ \Theta' = -\dfrac{\mathrm{Bi}}{A_2}(1-\Theta),\quad \Phi = 1 \quad \text{at} \quad \eta = 0 \\ f' \to 0,\quad \Theta \to 0,\quad \Phi \to 0 \quad \text{as} \quad \eta \to \infty \end{cases}$$

The dimensionless form of the governing equations is

$$\dot{u}_1 = u_2,$$

$$\dot{u}_2 = u_3,$$

$$\dot{u}_3 = -\frac{-u_2^2 + u_3u_1 + G_tu_4 + G_su_6 - Mu_2}{A_1\left(1+\frac{1}{\gamma}\right)},$$

$$\dot{u}_4 = u_5,$$

$$\dot{u}_5 = \frac{A_3}{A_2}[N_bu_7u_5 + N_t\ u_5^2 + A_1\ Ec\ u_3^2 + Pr\ Ec\ M\ u_2^2 + Pr\ u_1u_5],$$

$$\dot{u}_6 = u_7,$$

$$\dot{u}_7 = -\frac{N_t}{N_b}\dot{u}_5 - Sc\ u_1u_7.$$

with the conditions

$$u_1 = 0,\ \ u_2 = 1,\ \ u_5 = -\frac{\mathrm{Bi}}{A_2}(1-u_4),\quad u_6 = 1 \quad \text{at} \quad \eta = 0.$$
$$u_2 \to 0,\quad u_4 \to 0,\quad u_6 \to 0 \quad \text{as} \quad \eta \to \infty.$$

The set of nondimensional ordinary differential equations obtained from the governing equations was numerically computed through the **bvp4c** function in MATLAB, which employs a collocation method for boundary value problems. The boundary, conditions at $\eta = 0$ and $\eta \to \infty$ were incorporated to maintain accuracy in the computed outcomes. Initial guesses for the solution profiles were carefully chosen to facilitate convergence, given the nonlinearity of the equations. The solutions for primary velocity (f^'), secondary velocity (f), temperature (Θ), and concentration (Φ) were derived based on the magnetic field parameter (M), Eckert number (Ec), and nanoparticle volume fraction (Φ). The simulation relied on an iterative process to satisfy strict residual tolerances across the entire model. Running multiple iterations driven by MATLAB's solver drove down the residuals of the system equations and boundaries, establishing excellent numerical stability for the resulting trends. The baseline parameter values utilized in the computations are given as

$$\gamma = 0.10;\ Gt = 1.00;\ Gs = 1.00;\ M = 2.00;\ Nb = 0.10;\ Nt = 0.10;$$

$$Ec = 0.10;\ Pr = 4.00;\ Sc = 0.62;\ Bi = 0.10;\ \eta_\infty = 10.00;$$

The thermophysical properties of the nanofluid are also provided in Table 1.

Table 4.1: Thermophysical properties of the nanofluid

	$\rho(kg/m^3)$	$c_p(j/kgK)$	$\kappa(W/mK)$	Source
Fe_3O_4	5200	670.0	6.00	Ly et al., 2021
Fe_2O_3	5242	681	20	Giwa et al., 2021
Blood	1093	3210	0.451	Oke et al., 2023

4.2 Discussion of Results

The numerical simulations generated critical insights into the transport mechanics of the hydromagnetic hybrid nanofluid. Specifically, the analysis isolates the distinct roles of three core variables: the magnetic field parameter (M), the Eckert number (Ec), and the nanoparticle volume fraction (Φ) variables. Shifting these physical factors directly alters the resulting velocity profiles, temperature distributions, and localized concentration fields throughout the system. The magnetic field parameter (M) profoundly influences the system's overall dynamics by introducing a resistive Lorentz force that directly opposes the fluid flow. This drag creates substantial internal friction, which alters both the localized velocity patterns and the resulting temperature distribution. As plotted in Figures 4.1 and 4.2, intensifying the magnetic field causes a distinct decline in the magnitudes of both the primary and secondary velocity profiles. Mechanistically, this suppression occurs because the interaction between the moving, electrically conducting fluid and the magnetic field generates an electromagnetic damping effect. This Lorentz force acts as a retarding mechanism, draining kinetic energy from the system and dampening fluid motion. The observed effect exists in actual situations which generate beneficial results but simultaneously generates detrimental effects. The decreased fluid velocity in cooling systems allows the fluid to stay longer near heat exchangers which could lead to better heat transfer performance. The magnetic field strength creates obstacles for processes which need fast fluid movement because it affects their operational efficiency in chemical reactors and mixing systems. Increasing magnetic field strength results in a reduction of fluid velocities but the temperature and concentration profiles show opposite behavior according to Figures 4.3 and 4.4. The observed temperature rises stems from the fluid's enhanced ability to retain thermal energy. The magnetic field creates opposition to fluid movement which produces increased heat through the process of viscous dissipation that occurs within the fluid. The thermal energy which builds up from this process becomes useful for medical procedures which need exact temperature control in their thermal management systems. Magnetic field intensification generates a concentration gradient that leads to higher overall solutal retention across the fluid surface. This localized opposition to flow allows solutes to spread more uniformly, directly boosting reaction speeds in mass transfer-dependent systems. This effect hits maximum intensity under peak conditions, proving highly useful for stabilizing electrochemical cells and optimizing chemical synthesis pathways. In these setups, maintaining precise control over localized concentration gradients is the determining factor for maximizing chemical efficiency and total yield.

The Eckert number ((Ec)) quantifies the role of fluid viscosity in shaping both temperature profiles and velocity fields via viscous dissipation. As illustrated in Figures 4.5 and 4.6, there is a clear, direct correlation between an increasing Eckert number and the acceleration of both the primary and secondary velocity fields. The observed increase in velocity results from the conversion of kinetic energy into thermal energy, which enables better fluid flow. The temperature profile shows an increase in temperature values that match the rising Eckert numbers according to Figure 4.7. The process of viscous dissipation produces extra heat, which results in higher thermal energy levels within the fluid. The thermal elevation creates effects which reach past temperature measurement because Figure 4.8 shows that elevated Eckert numbers lead to increased concentration profiles. The system shows better solute transport because the increased fluid speed and stronger thermal energy work together to enhance the process.

The flow velocities, together with temperature and concentration profiles in fluid systems, experience major changes because of the amount of nanoparticles that exist in the solution. As illustrated in Figures 4.9 and 4.10, there is a noteworthy correlation between the nanoparticle volume fraction and the primary and secondary velocities of the flow. The improved fluid velocity results from nanoparticles, which show better thermal conductivity properties that enhance energy transfer in the fluid to produce faster fluid movement. The temperature profile shows an upward trend when the volume fraction of nanoparticles increases, according to Figure 4.11. The trend shows better heat transfer efficiency because nanoparticles optimize thermal performance for improved efficiency. The nanoparticles enhance thermal contact between particles which results in uniform fluid temperature distribution that engineers need for their thermal management work. The concentration profile shows a decrease in its values when the volume fraction of the solution increases according to Figure 4.12. The concentration gradient becomes smaller because nanoparticle concentrations rise which leads to this decrease in concentration. The presence of a higher volume fraction of nanoparticles tends to favour thermal diffusion over solutal diffusion, thereby disrupting the conventional concentration distribution.

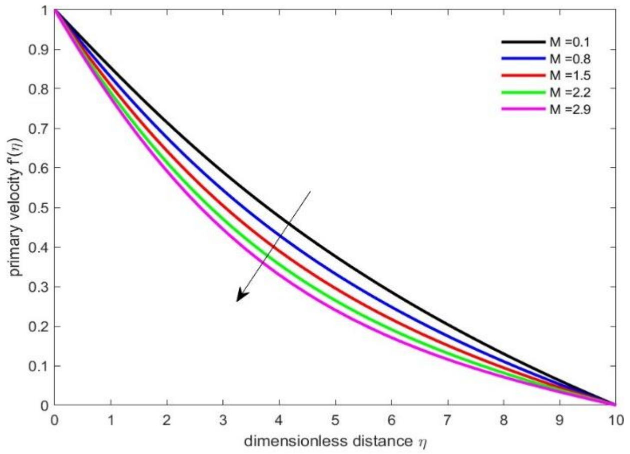

Figure 4.1: Primary velocity with Magnetic Field Strength

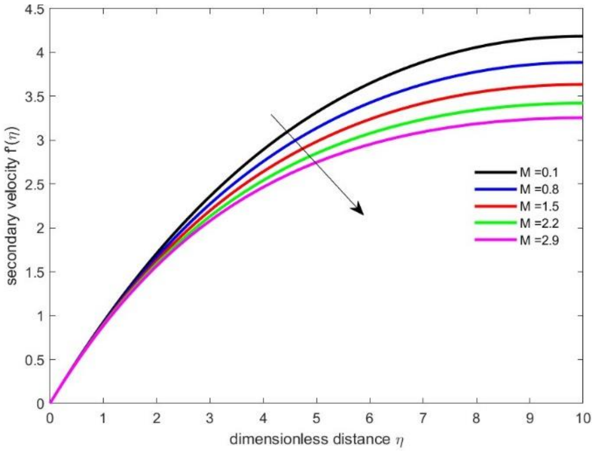

Figure 4.2: Secondary velocity with Magnetic Field Strength

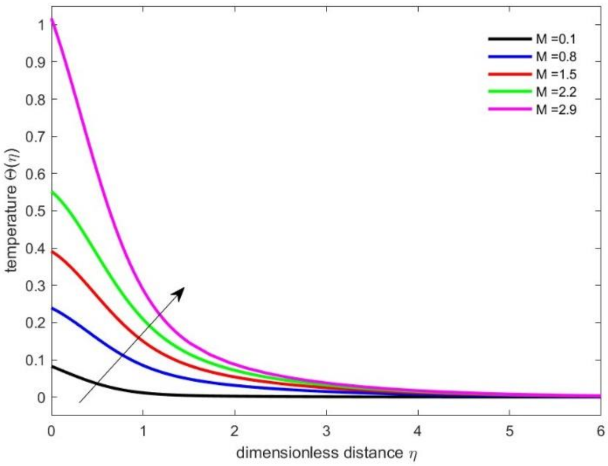

Figure 4.3: Temperature with Magnetic Field Strength

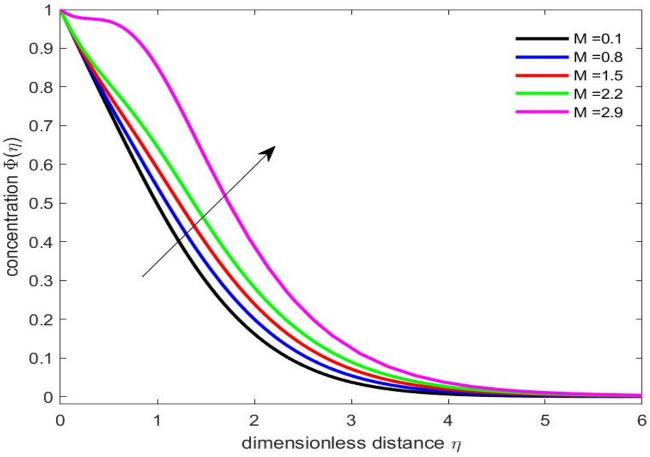

Figure 4.4: Concentration with Magnetic Field Strength

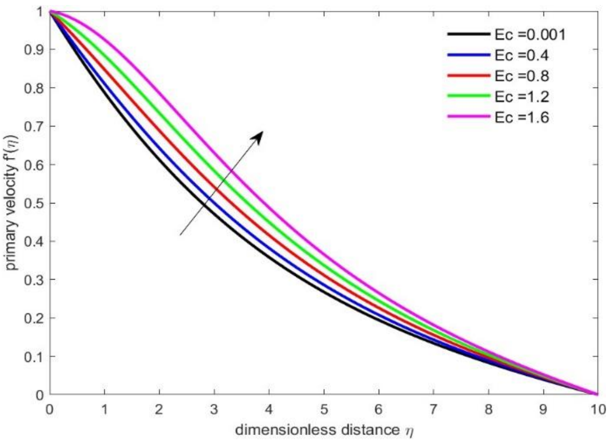

Figure 4.5: Primary velocity with Eckert number

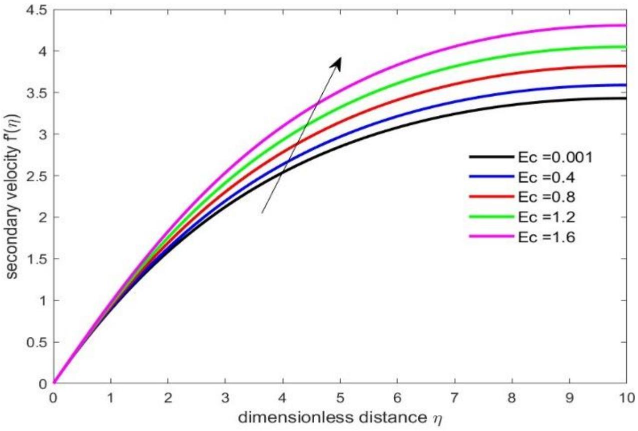

Figure 4.6: Secondary velocity with Eckert number

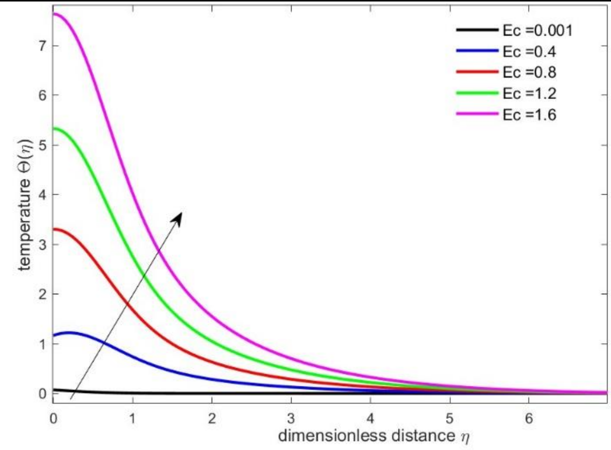

Figure 4.7: Temperature with Eckert number

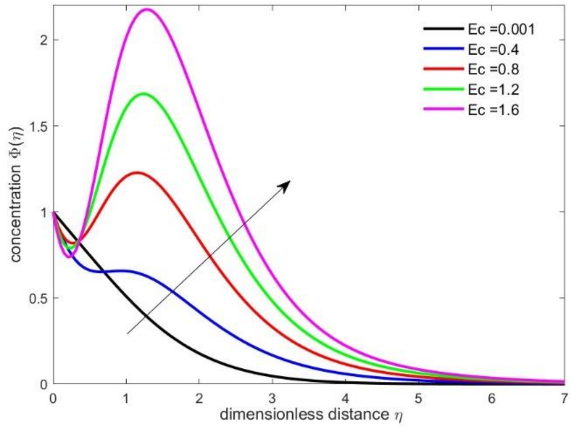

Figure 4.8: Concentration with Eckert number

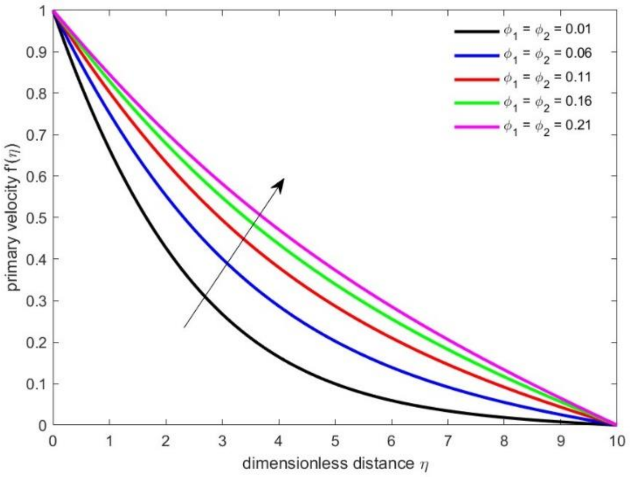

Figure 4.9: Primary velocity with volume fraction

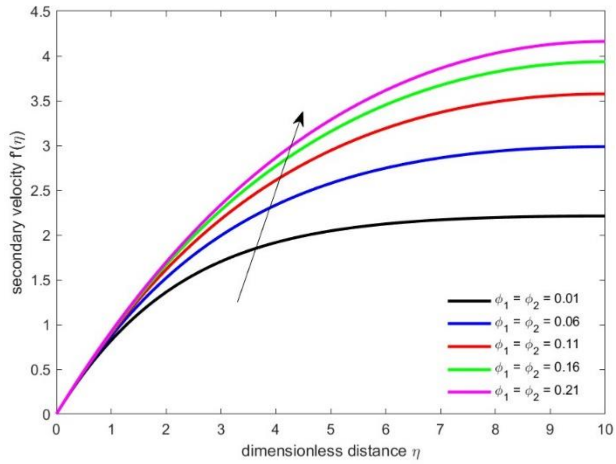

Figure 4.10: Secondary velocity with volume fraction

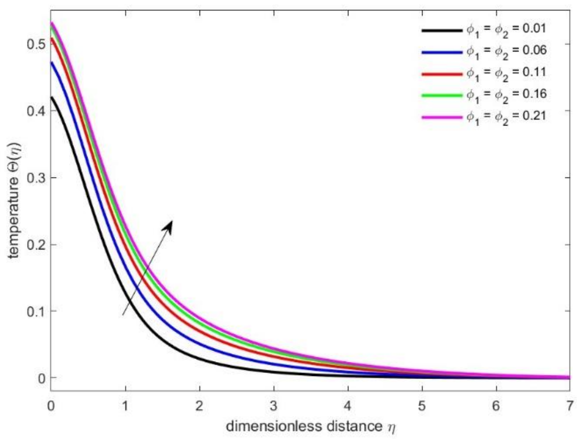

Figure 4.11: Temperature with volume fraction

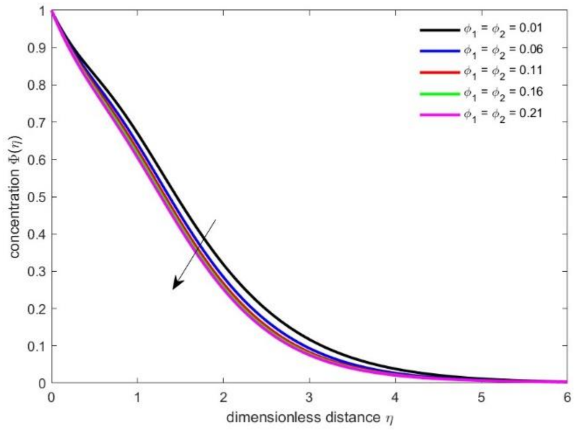

Figure 4.12: Concentration with volume fraction

CONCLUSION

The research investigated hydromagnetic flow patterns which occur when iron (II, III) oxide (Fe_3O_4) and iron (III) oxide (Fe_2O_3) nanoparticles are dispersed in human blood. The research studied how magnetic field strength and Eckert number and nanoparticle volume fraction affect both flow patterns and temperature and concentration distribution. The research findings effectively solved all the particular research questions which were established at the beginning of the investigation. The fundamental equations which describe hybrid nanofluids behavior were developed through applications of fluid mechanics and thermodynamics principles. The model consisted of four basic equations which handled continuity and momentum and energy and concentration behavior and incorporated magnetic field effects and buoyancy force impacts. The research achieves its first specific goal through the creation of a strong theoretical model which explains hybrid nanofluid behavior. The governing equations underwent dimensionless transformation through the application of similarity variables. The method successfully transformed the system of partial differential equations (PDEs) into ordinary differential equations (ODEs) which allowed for quick numerical solution methods. The successful conversion of the boundary conditions into dimensionless form demonstrates the power of similarity transformations in reducing complex, multi-variable fluid flow problems into streamlined mathematical systems. Simulating the resulting non-linear ODEs via MATLAB's bvp4c solver provided a clear mapping of how specific variables dictate fluid behavior. The numerical data shows that a stronger magnetic field induces a restrictive Lorentz force, which slows down primary and secondary velocities but drives up localized temperature and concentration profiles. Viscous dissipation, captured through the Eckert number, injects additional kinetic energy into the system, raising both fluid velocities and thermal readings while forcing concentration levels upward. Additionally, the nanoparticle volume fraction serves as a dual-edged variable; it successfully optimizes velocity and temperature outputs but causes the concentration profile to decline due to dominant thermal diffusion forces. Rather than just offering theoretical data, these finalized dynamics offer highly practical insights capable of advancing microfluidic drug delivery in oncology and optimizing high-heat industrial systems. The research results can help developers create better drug delivery systems and improve magnetic hyperthermia treatments and electromagnetic pump and cooling system performance.

RECOMMENDATION

The research results together with their scientific and practical value lead to the following recommendations which will direct upcoming investigations about hybrid nanofluids.

1. Future studies need to analyze hybrid nanofluid behavior through different nanoparticle combinations which include graphene and titanium dioxide (TiO2) and silver (Ag) and traditional Fe_2O_3 and Fe_3O_4. materials. The research needs to study hybrid nanofluid movement through non-Newtonian fluids because blood displays non-Newtonian behavior when it encounters particular conditions.
2. The numerical results deliver important information but experimental testing must occur to confirm the theoretical models. The research team should create laboratory environments which duplicate the study parameters through magnetic field control and blood-mimicking fluid suspension of hybrid nanoparticles. The solution of hybrid nanofluid problems will achieve better efficiency and precision through machine learning and artificial intelligence-based simulations which use advanced numerical methods.
3. Researchers need to develop optimization models which will determine the best parameter settings for particular uses of hybrid nanofluids including cooling systems and magnetic fluid seals. The research will achieve better results through application-specific studies which will focus on magnetic cooling systems and electromagnetic pumps and drug delivery mechanisms.

REFERENCES

1. Alfvén, H. (1942). Existence of Electromagnetic-Hydrodynamic Waves. *Nature*, 150(3805):405–406.
2. Bhatti, M. M., Sait, S. M., & Ellahi, R. (2022). Magnetic nanoparticles for drug delivery through tapered stenosed artery with blood based non-Newtonian fluid. *Pharmaceuticals*, *15*(11), 1352.
3. Gireesha, B. J., & Sindhu, S. (2020). MHD natural convection flow of Casson fluid in an annular microchannel containing porous medium with heat generation/absorption. *Nonlinear engineering*, *9*(1), 223-232.
4. Giwa, S. O., Sharifpur, M., Ahmadi, M. H., Sohel Murshed, S. M., & Meyer, J. P. (2021). Experimental investigation on stability, viscosity, and electrical conductivity of water-based hybrid nanofluid of MWCNT-Fe2O3. *Nanomaterials*, *11*(1), 136.
5. Hayat, T. and Nadeem, S. (2017). Heat transfer enhancement with ag–CuO/water hybrid nanofluid. 7:2317–2324.
6. Islam, S., Dawar, A., Shah, Z., & Tariq, A. (2021). Cattaneo–Christov theory for a time-dependent magnetohydrodynamic Maxwell fluid flow through a stretching cylinder. *Advances in Mechanical Engineering*, *13*(7), 16878140211030152.
7. Juma, B. A., Oke, A. S., Mutuku, W. N., Ariwayo, A. G., & Ouru, O. J. (2022). Dynamics of Williamson fluid over an inclined surface subject to Coriolis and Lorentz forces. *Engineering and Applied Science Letter*, *5*(1), 37-46.
8. Krishnamurthy, M. R., Prasannakumara, B. C., Gireesha, B. J., & Gorla, R. S. R. (2016). Effect of chemical reaction on MHD boundary layer flow and melting heat transfer of Williamson nanofluid in porous medium. *Engineering Science and Technology, an International Journal*, *19*(1), 53-61.
9. Lv, Y. P., Algehyne, E. A., Alshehri, M. G., Alzahrani, E., Bilal, M., Khan, M. A., & Shuaib, M. (2021). Numerical approach towards gyrotactic microorganisms hybrid nanoliquid flow with the hall current and magnetic field over a spinning disk. *Scientific Reports*, *11*(1), 8948.
10. Mahabaleshwar, U. S., Nagaraju, K. R., Kumar, P. V., Nadagouda, M. N., Bennacer, R., & Sheremet, M. A. (2020). Effects of Dufour and Soret mechanisms on MHD mixed convective-radiative non-Newtonian liquid flow and heat transfer over a porous sheet. *Thermal Science and Engineering Progress*, *16*, 100459.
11. Maïga, S. E. B., Nguyen, C. T., Galanis, N., & Roy, G. (2004). Heat transfer behaviours of nanofluids in a uniformly heated tube. *Superlattices and Microstructures*, *35*(3-6), 543-557. Othman, M. N., Jedi, A., and Bakar, N. A. A. (2021). MHD flow and heat transferof hybrid nanofluid over an exponentially shrinking surface with heat source/sink. 11(17):8199.
12. Oke, A. S., Juma, B. A., & Oyem, A. O. (2023). Hydromagnetic flow of Casson fluid carrying CNT and graphene nanoparticles in armory production. *WSEAS Transactions on Fluid Mechanics*, *18*, 123-134.
13. Pak, B. C., & Cho, Y. I. (1998). Hydrodynamic and heat transfer study of dispersed fluids with submicron metallic oxide particles. *Experimental Heat Transfer an International Journal*, *11*(2), 151-170.
14. Shakil, M. S., Hasan, M. A., & Sarker, S. R. (2019). Iron oxide nanoparticles for breast cancer theranostics. *Current drug metabolism*, *20*(6), 446-456.
15. Sheikholeslami, M., Mehryan, S., Shafee, A., and Sheremet, M. A. (2019). Variable magnetic forces impact on magnetizable hybrid nanofluid heat transfer through a circular

cavity.277:388–396.

16. Shi, Y., Sun, Y., Yu, J., Ding, C., Wang, Z., Wang, C... & Huang, Y. (2017). China expert's consensus on the diagnosis and treatment of advanced stage primary lung cancer (2016 version). *Asia-Pacific Journal of Clinical Oncology*, *13*(1), 87-103.
17. Subhani, M. and Nadeem, S. (2018). Numerical analysis of micropolar hybrid nanofluid.
18. Suresh, S., Venkitaraj, K., Selvakumar, P., and Chandrasekar, M. (2011). Synthesis of al2o3–cu/water hybrid nanofluids using two-step method and its thermophysical properties. 388 (1-3):41–48.
19. Tassaddiq, A., Khan, S., Bilal, M., Gul, T., Mukhtar, S., Shah, Z., and Bonyah, E. (2020). Heat and mass transfer together with hybrid nanofluid flow over a rotating disk. 10(5):055317.

Statement of problem

We considered the generalized Optimal Control problem given below;

$$\max(\min) J(u) = \int_{t_0}^{T} F(t, x_1(t), x_2(t), \ldots, x_n(t), u(t))\, dt \quad (1)$$

$$\text{subject to : } \dot{x}_1 = g_1(t, x_1(t), x_2(t), \ldots, x_n(t), u(t)) \quad (2)$$

$$\dot{x}_2 = g_2(t, x_1(t), x_2(t), \ldots, x_n(t), u(t)) \quad (3)$$

$$\ldots$$

$$x_n = g_n(t, x_1(t), x_2(t), \ldots, x_n(t), u(t)) \quad (4)$$

$$u_{\min} \leq u \leq u_{\max} \quad (5)$$

where $(x_1(t_0), x_2(t_0), \ldots, x_n(t_0)) = (0,0,\ldots,0)^T \in \mathbf{R}^n$.

The Hamiltonian of the constrained optimal control problem is written as

$$H = F(t, x_1(t), x_2(t), \ldots, x_n(t), u(t)) + \sum_{i=1}^{n} \lambda_i g_i(t, x_1(t), x_2(t), \ldots, x_n(t), u(t)), \quad (6)$$

and the optimality, adjoint and transversality conditions are expressed below respectively as

(Optimality) $$\frac{\partial H}{\partial u} = \frac{\partial F}{\partial u} + \sum_{i=1}^{n} \lambda_i \frac{\partial g_i}{\partial u} \quad (7)$$

(Adjoint) $$\dot{\lambda}_i = -\frac{\partial H}{\partial x_i} = -\frac{\partial F}{\partial x_i} - \sum_{i=1}^{n} \lambda_i \frac{\partial g_i}{\partial x_i}, \quad (8)$$

(Transversality), $$\lambda_i(T) = 0 \ \ \forall\ i = 1, 2, \ldots, n \quad (9)$$

1.2: 6th Order Runge-Kutta Scheme

The 7-stage Runge-Kutta of order 6 (RK6) iterative scheme was considered for the development of the forward-backward sweep Algorithm for the solution of Optimal control problems[11]. The RK6 enhances the level of accuracy of the results of the optimal control problem with the developed algorithm[12].

$$\begin{aligned}
K_1 &= hf(t_k, x_k), \\
K_2 &= hf\left(t_k + \frac{h}{4}, x_k + \frac{K_1}{4}\right), \\
K_3 &= hf\left(t_k + \frac{h}{4}, x_k + \frac{K_1 + K_2}{8}\right), \\
K_4 &= hf\left(t_k + \frac{h}{2}, x_k + \frac{-5K_2 + 8K_3}{6}\right), \\
K_5 &= hf\left(t_k + \frac{3h}{4}, x_k + \frac{K_1 + K_2 + 4K_4}{8}\right), \\
K_6 &= hf\left(t_k + \frac{3h}{4}, x_k + \frac{3K_2 + 2K_3 - K_4 + 2K_5}{8}\right), \\
K_7 &= h\,f\left(t_k + h, x_k + \frac{K_1 - 2K_2 + 4K_3 + 4K_6}{7}\right)
\end{aligned}$$

$$x_{k+1} = x_k + \frac{7K_1 + 32K_3 + 12K_4 + 16K_5 + 16K_6 + 7K_7}{90}$$

1.3: Forward-Backward Sweep Method

The derivation of the forward-backward sweep requires the discretization of state, control, and adjoint variables along the knots $t_0 \le t_1 \le t_2 \le \cdots \le t_N$, such that $x_i^k = x_i(t_0 + kh)$,

$u_s^k = u_s(t_0 + kh)$, and $\lambda_{ji} = \lambda_i(t_0 - jh)$ for $t_k = t_0 + kh$ and $h = (T - t_0)/N$ is the

Step-length with N number of grid-points.Therefore, for any argument x_i in the state vector ($x_i^k, x_2^k, \cdots, x_n^k) \in \mathbb{R}^n$ and a unit adjoint variable u_s for s ∈ {1,2,⋯ ,m} and the forward sweep of the state variable using the RK6 method is written as:

$$K_{i1} = hg_1(t_k, x_i^k, u_s(k)), \tag{10}$$

$$K_{i2} = hg_2(t_k + \frac{h}{4}, x_i^k + \frac{K_1}{4}, u_s(t_k + \frac{h}{4})), \tag{11}$$

$$K_{i3} = hg_3(t_k + \frac{h}{4}, x_i^k + \frac{1}{8}(K_1 + K_2),\ u_s(t_k + \frac{h}{4})), \tag{12}$$

$$K_{i4} = hg_4(t_k + \frac{h}{2}, x_i^k + \frac{1}{6}(-5K_2 + 8K_3), u_s(t_k + \frac{h}{2})), \tag{13}$$

$$K_{i5} = hg_5(t_k + \frac{3h}{4}, x_i^k + \frac{1}{8}(K_1 + K_2 + 4K_3), u_s(t_k + \frac{3h}{4})), \tag{14}$$

$$K_{i6} = hg_6(t_k + \frac{3h}{4}, x_i^k + \frac{1}{8}(3K_2 + 2K_3 - K_4 + 2K_5), u_s(t_k + \frac{3h}{4})) \tag{15}$$

$$K_{i7} = h\, g_7\left(t_k + h, x_i^k + \frac{1}{7}(K_1 - 2K_2 + 4K_3 + 4K_6),\ u_s(t_k + h)\right) \tag{16}$$

$$x_i^{k+1} = x_i^k + \frac{7K_1 + 32K_3 + 12K_4 + 16K_5 + 16K_6 + 7K_7}{90}. \tag{17}$$

for the subscript of each argument *i*= 1,2,⋯ ,*n*, *r* = 1,2,⋯ ,*m*, the counter *k* = 1,2,⋯ ,*N*. and the functions g_l, l = 1, 2⋯7 are once continuously differentiable within the time interval [$t_0, T]$ $\left(\text{i.e } \frac{\partial g_l}{\partial x_i} \in C^1[t_0, T]\right)$ and K_{il} denoting the dynamical function of the *i*−th component (argument) and the *l*−th stage. For the control characterization, the optimal variable is derived using the optimality condition $\frac{\partial H}{\partial u_r}$= 0 such that

$$u_r^* = \min\{\max\{u_{min}, u_r, \}, u_{max}\} \tag{18}$$

The interpolating polynomial or spline [8] of the control variable $u_s(.)$ can be computed as the formula;

$$u(t \underset{-}{+} \frac{ah}{b}) = \frac{au(t \underset{-}{+} h) + (b-a)u(t)}{b} \tag{19}$$

The control variable for the forward(+) and backward (-) sweep are approximated respectively as follows;

$$u(t \underset{-}{+} \frac{ah}{b}) \approx \begin{cases} \frac{u(t \underset{-}{+} h) + 3u(t)}{4} & a = 1, b = 4 \\ \frac{u(t \underset{-}{+} h) + u(t)}{2} & a = 1, b = 2 \\ \frac{3u(t \underset{-}{+} h) + u(t)}{4} & a = 3, b = 4 \end{cases} \tag{20}$$

The backward sweep of the adjoint variables using the proposed RK6 method requires the discretization of the adjoint such that for any argument $\lambda_l^j \in (\lambda_1^j, \lambda_2^j, \cdots, \lambda_n^j) \in \mathbb{R}^n$ with a specific control variable u_s attached to each state equation is expressed thus:

$$\dot{\lambda}_i = -\frac{\partial H}{\partial x_i}(t, \lambda_i, x_i, u_s), \quad i = 1, 2, \ldots, n. \tag{21}$$

Deploying the 7-stage RK6 numerical scheme in the discretization of the backward sweep for the adjoint variables yields the following:

$$K_{i1} = -\frac{\partial H}{\partial x_i}(t_j, \lambda_i^j, x_i, u_s(j)), \tag{22}$$

$$K_{i2} = -\frac{\partial H}{\partial x_i}(t_j + \frac{h}{4}, \lambda_i^j + \frac{K_1}{4}, x_i^j + \frac{K_1}{4}, u_s(t_j + \frac{h}{4})), \tag{23}$$

$$K_{i3} = -\frac{\partial H}{\partial x_i}(t_j + \frac{h}{4}, \lambda_i^j + \frac{1}{8}(K_1 + K_2), x_i^j + \frac{1}{8}(K_1 + K_2), u_s(t_j + \frac{h}{4})), \tag{24}$$

$$K_{i4} = -\frac{\partial H}{\partial x_i}(t_j + \frac{h}{2}, \lambda_i^j + \frac{1}{6}(-5K_2 + 8K_3), x_i^j + \frac{1}{6}(-5K_2 + 8K_3), u_s(t_j + \frac{h}{2})), \tag{25}$$

$$K_{i5} = -\frac{\partial H}{\partial x_i}(t_j + \frac{3h}{4}, \lambda_i^j + \frac{1}{8}(K_1 + K_2 + 4K_3), x_i^j + \frac{1}{8}(K_1 + K_2 + 4K_3), u_s(t_j + \frac{3h}{4})), \tag{26}$$

$$K_{i6} = -\frac{\partial H}{\partial x_i}(t_j + \frac{3h}{4}, \lambda_i^j + \frac{1}{8}(3K_2 + 2K_3 - K_4 + 2K_5), x_i^j + \frac{1}{8}(3K_2 + 2K_3 - K_4 + 2K_5), u_s(t_j + 3h4)), \tag{27}$$

$$K_{i7} = -\frac{\partial H}{\partial x_i}(t_j + h, \lambda_i^j + \frac{1}{7}(K_1 - 2K_2 + 4K_3 + 4K_6), x_i^j + \frac{1}{7}(K_1 - 2K_2 + 4K_3 + 4K_6), u_s(t_j + h)), \tag{28}$$

$$\lambda_i^{j-1} = \lambda_i^j - \frac{h}{90}(7K_1 + 32K_3 + 12K_4 + 16K_5 + 16K_6 + 7K_7). \tag{29}$$

1.4: RK6 Forward-Backward Algorithm for Optimal Control Problem

Step 1: Initialization Input

$x_i(t_0) = x_i^0, \quad \lambda_i(N) = 0 \ \forall i = 1, 2, \cdots, n, \ T, \ t_0, \ u_r(t_0) = u_r^0, \forall r = 1, 2, \cdots, m$

Step 2: Forward Sweep for state variables

Compute while $k = 0,1,2,...,N$ do x_i^{i+1} from equations (10) to (17) respectively and sequentially.

Step 3: Backward Sweep for adjoint variables

Set $j = N + 2 - i$ and compute λ_i^{j-1} from equations (22) to (29) respectively *Step 4: Control Characterization* Compute control within bounds $u_r^* = \min\{\max\{u_{min}, u_r, \}, \ u_{max}\} \text{ for } r = 1, \cdots, m$ from equation (18)

Step 5: Termination criteria

If termination conditions are met go to step 6 otherwise step 7

Step 6: Output $x^k_i, \lambda^j_i, u^*_i (\forall i, j)$ and end function *Step 7: Return* Repeat step 2

2: Numerical simulations: Implementation and Results

Example 1: Considering the optimal control problem below

$$\text{Min } J[u] = \min \int_0^1 u(t)2 \, dt,$$

$$x'(t) = x(t) + u(t), \tag{30}$$

$$x(0) = 1, \ x(1) \text{ free.}$$

The Hamiltonian function H is defined as $H = u(t)^2 + \lambda(t)\cdot(x(t)+u(t))$ where $\lambda(t)$ is the adjoint variable (or costate). Using the optimality adjoint and transversality conditions yields the analytical (exact) optimal solution below:

$$x^*(t) = e^t, \qquad u^*(t) = 0. \tag{31}$$

The optimal control obtained using the optimality condition, $\frac{\partial H}{\partial u} = 0$, is given by

$$\begin{aligned} u^*(t) &= -\frac{\lambda(t)}{2}, \\ &= \min\left(u_{\max},\, \max\left(u_{min}, -\frac{\lambda(t)}{2}\right)\right) \end{aligned} \tag{32}$$

ascertained to be minimum since $\frac{\partial^2 H}{\partial u^2} = 2 > 0.$

The derived costate equation using the adjoint conditions, $\lambda'(t) = -\frac{\partial H}{\partial I(t)}$, given by:

$$\lambda'(t) = -\lambda(t), \quad \lambda(T) = 0 \tag{33}$$

Applying the forward Euler, RK4 and the proposed RK6 forward -backward sweep methods (i.e RK4FBSM and proposed RK6FBSM respectively) yields the results below.

Table1: Result of State variable for example 1

S/N	Exact	Euler		RK4FBSM		Proposed RK6FBSM	
	x_A	x_E	$\lvert x_A - x_E\rvert$	$xK4$	$\lvert xA - xK4\rvert$	$xK6$	$\lvert xA - xK6\rvert$
1	1.1051709181	1.1111111111	$5.9401930000 \times 10^{-3}$	1.1051708333	8.47000×10^{-8}	1.1051709181	0.00000×10^0
2	1.2214027582	1.2345679012	$1.3165143100 \times 10^{-2}$	1.2214025709	1.87300×10^{-7}	1.2214027582	0.00000×10^0
3	1.3498588076	1.3717421125	$2.1883304900 \times 10^{-2}$	1.3498584971	3.10500×10^{-7}	1.3498588076	0.00000×10^0
4	1.4918246976	1.5241579028	$3.2333205100 \times 10^{-2}$	1.4918242401	4.57600×10^{-7}	1.4918246977	0.00000×10^0
5	1.6487212707	1.6935087808	$4.4787510100 \times 10^{-2}$	1.6487206386	6.32100×10^{-7}	1.6487212707	0.00000×10^0
6	1.8221188004	1.8816764232	$5.9557622800 \times 10^{-2}$	1.8221179621	8.38300×10^{-7}	1.8221188004	0.00000×10^0
7	2.0137527075	2.0907515813	$7.6998873800 \times 10^{-2}$	2.0137516266	1.08090×10^{-6}	2.0137527075	0.00000×10^0
8	2.2255409285	2.3230573125	$9.7516384100 \times 10^{-2}$	2.2255395633	1.36520×10^{-6}	2.2255409285	0.00000×10^0
9	2.4596031112	2.5811747917	$1.2157168060 \times 10^{-1}$	2.4596014138	1.69740×10^{-6}	2.4596031112	0.00000×10^0

10	2.7182818285	2.8679719908	$1.4969016230\times10^{-1}$	2.7182797441	2.08430×10^{-6}	2.7182818285	0.00000 $\times10^{0}$

Table 1: $|x_A - x_E|$, $|x_A - x_{K4}|$and$|x_A - x_{K6}|$ ≡ errors of Euler RK4 & RK6 respectively

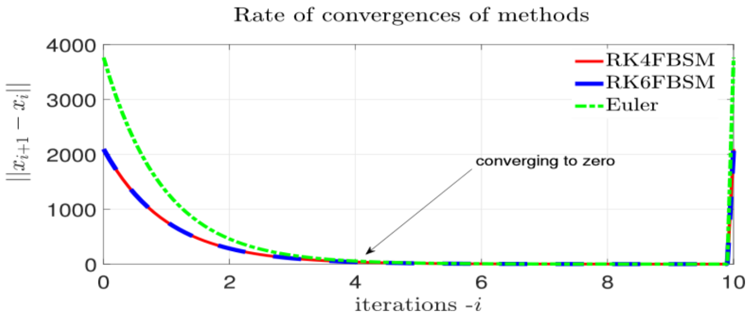

Figure 1: Rate of convergence in 10 iters.

Example 2: Considering the SIS Model with Treatment [9]

$$\begin{aligned} \min C[u] &= \int_0^T \omega_1 I(t) + u^2(t))\, dt, \\ s.t : \dot{I}(t) &= \beta \ \ (N - I(t))I(t) - (\mu + \gamma)I(t) - u(t)I(t) \end{aligned} \quad (34)$$

(35)

$$I(0) \quad = \quad I_0, I(T) free. \quad (36)$$

The Hamiltonian is given by:

$H(I(t),u(t),\lambda(t)) = \omega_1 I(t) + u^2(t) + \lambda(t)(\beta(N - I(t))I(t) - (\mu + \gamma)I(t) - u(t)I(t)$(37) The optimal control obtained using the optimality condition, $\frac{\partial H}{\partial u} = 0$, is given by

$$\begin{aligned} u^*(t) &= \frac{\lambda(t)I(t)}{2}, \\ &= \min\left(u_{\max}, \max\left(u_{min}, \frac{\lambda(t)I(t)}{2}\right)\right). \end{aligned} \quad (38)$$

ascertained to be minimum since $\frac{\partial^2 H}{\partial u^2} = 2 > 0.$

The derived co-state equation using the adjoint conditions, $\lambda'(t) = -\frac{\partial H}{\partial I(t)}$, given by:

$\lambda'(t) = -\omega_1 - \lambda(t)\beta(N - I(t)) - \beta I(t) - (\mu + \gamma) - u(t), \lambda(T) = 0$ (39)

Applying the forward Euler, RK4 and the proposed RK6 forward -backward sweep methods (i.e RK4FBSM and proposed RK6FBSM respectively) also yields the results in Table 2 below using the following parameters: $\beta = 0.05$, $\mu = 0.01$, $\gamma = 0.5$, $N = 100$, $\omega_1 = 1$ and $T = 1$.

Table 2: Result of State and Control variables for example 2

S/N	Euler		convergence		Proposed RK6FBSM	
	x_E	u_E	$xK4$	$uK4$	$xK6$	$uK6$
1	10.0000000000	5.2355651638	10.0000000000	4.5926947060	10.0000000000	4.6363573386
2	8.7650656568	4.6326137300	9.5613737942	4.3167361686	9.5464589222	4.3768363778
3	8.2556597311	4.1600567381	9.4089685710	4.0418362859	9.3440040276	4.1061078144
4	8.1851105244	3.7431700492	9.5201882548	3.7594888052	9.3763319652	3.8164326820
5	8.4592147545	3.3460084781	9.9038244602	3.4602903181	9.6519009702	3.4992076079
6	9.0673116818	2.9449889133	10.6018768364	3.1325900058	10.2060033528	3.1440596831
7	10.0557266500	2.5197980734	11.7007294372	2.7604692418	11.1093962855	2.7374992954
8	11.5303031948	2.0484433716	13.3574883436	2.3201655255	12.4871637697	2.2605946027
9	13.6800933636	1.5026879752	15.8577984930	1.7728678617	14.5571182701	1.6844954512
10	16.8306930352	0.8415968385	19.7510850824	1.0482398348	17.7109254612	0.9609642283
11	21.5547425985	0.0000000000	26.2132226347	0.0000000000	22.7016008493	0.0000000000

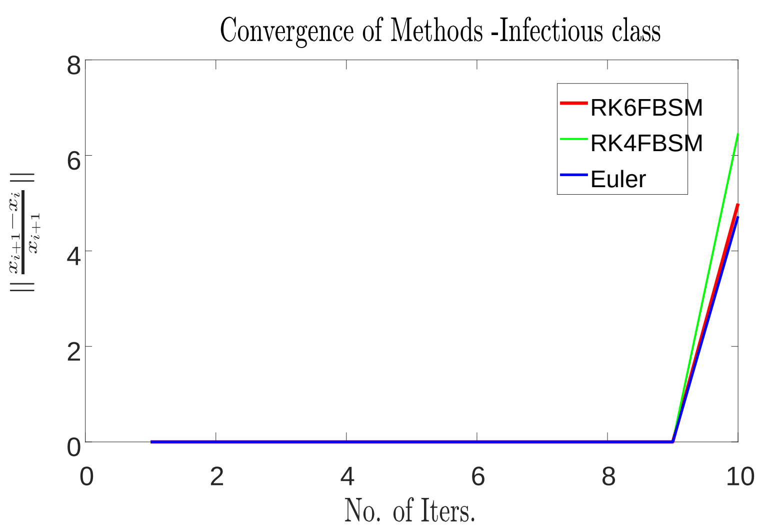

Figure 2: Rate of convergence in 10 iterations.

Example 3: We considered the model on optimal control and comprehensive cost effectiveness analysis for COVID-19 [2]

$$J(u_1,u_2,u_3,u_4) := \min \int_0^T \left[A_1E + A_2I + A_3A + A_4B + \frac{1}{2}\sum_{i=1}^{4} D_i u_i^2(t)\right] dt \tag{40}$$

Subject to the non-autonomous system below

$$\begin{cases} \frac{dS}{dt} &= \Lambda - (1-u_1(t))\left(\frac{\beta_1 E + \beta_2 I + \beta_3 A}{N}\right) S - (1-u_1(t)-u_2(t))\beta_4 \frac{B}{N} S - dS, \\ \frac{dE}{dt} &= (1-u_1(t))\left(\frac{\beta_1 E + \beta_2 I + \beta_3 A}{N}\right) S + (1-u_1(t)-u_2(t))\beta_4 \frac{B}{N} S - (\delta + d)E, \\ \frac{dI}{dt} &= (1-\tau)\delta E - (d + d_1 + \gamma_1)I, \\ \frac{dA}{dt} &= \tau\delta E - (d+\gamma_2)A, \\ \frac{dR}{dt} &= \gamma_1 I + \gamma_2 A - dR, \\ \frac{dB}{dt} &= (1-u_3(t))(\psi_1 E + \psi_2 I + \psi_3 A) - (u_4(t) + \phi)B, \end{cases} \tag{41}$$

where $A_i > 0 (i = 1,2,3,4)$. The derived adjoint equations were

$$\begin{cases} \frac{d\lambda_1}{dt} = (\lambda_1 - \lambda_2)((1-u_1)\left(\frac{\beta_1 E^* + \beta_2 I^* + \beta_3 A^*}{N^2}\right)(E^* + I^* + A^* + R^*)) + \\ (\lambda_1 - \lambda_2)(1-u_1-u_2)\beta_4 \frac{B^*}{N^2}(E^* + I^* + A^* + R^*) + \lambda_1 d, \\ \frac{d\lambda_2}{dt} = -A_1 + (\lambda_1 - \lambda_2)(1-u_1)S^*\left(\frac{(S^*+I^*+A^*+R^*)\beta_1 - (\beta_2 I^* + \beta_3 A^*)}{N^2}\right) + \\ (\lambda_2 - \lambda_1)(1-u_1-u_2)\beta_4 \frac{B^* S^*}{N^2} + (\delta + d)\lambda_2 - \lambda_2(1-\tau)\delta\lambda_3 - \tau\delta\lambda_4 - (1-u_3)\psi_1\lambda_6 \\ \frac{d\lambda_3}{dt} = -A_2 + (\lambda_1 - \lambda_2)(1-u_1)S^*\left(\frac{(S^*+E^*+A^*+R^*)\beta_2 - (\beta_1 E^* + \beta_3 A^*)}{N^2}\right) + \\ (\lambda_2 - \lambda_1)(1-u_1-u_2)\beta_4 \frac{B^* S^*}{N^2} + (\delta + d_1 + \gamma_1)\lambda_3 - \gamma_1\lambda_5 - (1-u_3)\psi_2\lambda_6, \\ \frac{d\lambda_4}{dt} = -A_3 + (\lambda_1 - \lambda_2)(1-u_1)S^*\left(\frac{(S^*+E^*+I^*+R^*)\beta_3 - (\beta_1 E^* + \beta_2 I^*)}{N^2}\right) + \\ (\lambda_2 - \lambda_1)(1-u_1-u_2)\beta_4 \frac{B^* S^*}{N^2} + (d_1 + \gamma_2)\lambda_4 - \gamma_2\lambda_5 - (1-u_3)\psi_3\lambda_6, \\ \frac{d\lambda_5}{dt} = (\lambda_2 - \lambda_1)(1-u_1)\left(\frac{(\beta_1 E^* + \beta_2 I^* + \beta_3 A^*)S^*}{N^2}\right) + \\ (\lambda_2 - \lambda_1)(1-u_1-u_2)\beta_4 \frac{S^*}{N^2} + \lambda_5 d, \\ \frac{d\lambda_6}{dt} = -A_4 + (\lambda_1 - \lambda_2)(1-u_1-u_2)\beta_4 \frac{S^*}{N} + (u_4 + \phi)\lambda_6 d, \end{cases} \tag{42}$$

while the optimal control characterizations were;

$$\begin{aligned} u_1^*(t) &= \min\left\{\max\left\{0, \frac{(\lambda_2 - \lambda_1)(\beta_1 E^* + \beta_2 I^* + \beta_3 A^* + \beta_4 B^*)S}{D_1 N}\right\}, u_{1\max}\right\} \\ u_2^*(t) &= \min\left\{\max\left\{0, \frac{(\lambda_2 - \lambda_1)\beta_4 B^* S^*}{D_2 N}\right\}, u_{2\max}\right\}, \\ u_3^*(t) &= \min\left\{\max\left\{0, \frac{\lambda_6(\psi_1 E^* + \psi_2 I^* + \psi_3 A^*)}{D_3}\right\}, u_{3\max}\right\}, \\ u_4^*(t) &= \min\left\{\max\left\{0, \frac{\phi B^* \lambda_6}{D_4}\right\}, u_{4\max}\right\}. \end{aligned} \tag{43}$$

Simulating with the following parameters $\beta_1 = 0.1233; \beta_2 = 0.0542; \beta_3 = 0.0020; \beta_4 = 0.1101; \delta = 0.1980; \tau = 0.3085; d = 1/(74.87 * 365); d_1 = 0.0104; \gamma_1 = 0.3680; \gamma_2 = 0; \psi_1 = 0.2574; \psi_2 = 0.2798; \psi_3 = 0.1584; \phi = 0.3820$ yields the results below.

Table 3: Convergence analysis of State variable ($E(t)$) for example 3

S/N	Euler		RK4FBSM		Proposed RK6FBSM	
	E_E	$\lVert\frac{E_{i+1}-E_i}{E_{i+1}}\rVert$	$EK4$	$\lVert\frac{E_{i+1}-E_i}{E_{i+1}}\rVert$	$EK6$	$\lVert\frac{E_{i+1}-E_i}{E_{i+1}}\rVert$
1	1.5000000000	-	1.5000000000		1.5000000000	

11	1.4586854415	2.7646377×10^{-3}	1.4582818367	2.7890189×10^{-3}	1.4581829510	2.7953366×10^{-3}
21	1.4194850125	2.6987961×10^{-3}	1.4187988721	2.7167244×10^{-3}	1.4186243717	2.7216273×10^{-3}
31	1.3821955578	2.6394372×10^{-3}	1.3813219909	2.6520393×10^{-3}	1.3810945185	2.6556630×10^{-3}
41	1.3466385402	2.5859736×10^{-3}	1.3456514066	2.5942269×10^{-3}	1.3453892655	2.5968128×10^{-3}
51	1.3126570130	2.5378496×10^{-3}	1.3116129021	2.5425930×10^{-3}	1.3113294894	2.5443931×10^{-3}
61	1.2801128162	2.4946384×10^{-3}	1.2790541427	2.4967666×10^{-3}	1.2787595421	2.4977039×10^{-3}
71	1.2488168407	2.4685349×10^{-3}	1.2477535795	2.4713852×10^{-3}	1.2474913995	2.4675198×10^{-3}
81	1.2184644912	2.4616005×10^{-3}	1.2173844274	2.4656931×10^{-3}	1.2171894367	2.4600497×10^{-3}
91	1.1893046217	2.3341404×10^{-3}	1.1885613052	2.2797627×10^{-3}	1.1883097475	2.2930852×10^{-3}
101	1.1685184378	1.2045593×10^{-3}	1.1684734094	1.2114794×10^{-3}	1.1676305020	1.2714446×10^{-3}

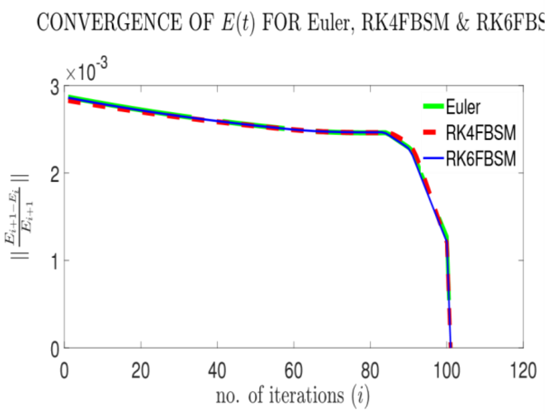

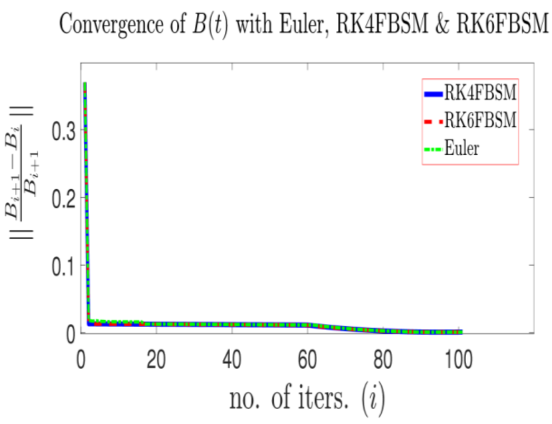

Fig. 3: Convergence of $E(t)$ in 101 iterations. Fig 4: Convergence of $B(t)$ in 101 iterations.

DISCUSSION OF RESULTS

In example 1, the rate of convergence of the 3 methods: Euler, RK4 and Rk6 were compared on the state variable as demonstrated on table 1. It was discovered that the rate of convergence of the RK6 compares favorably with RK4 with higher level of accuracy after 10 iterations. In similar manner, Table 2 and 3 were used to compare the Iterates for the Euler, RK4 and RK6 forward-backward sweep methods on the state variables of examples 2 and 3 respectively. Figures 2, 3 and 4 were used to illustrate the rate of convergences which shows that the RK6FBSM performs excellently well although the computational efforts is more in terms of rigors of coding and process time.

CONCLUSION

The adaptation of the 6th order Runge-Kutta forward-backward sweep algorithm for solving generalized optimal control problems with bounded control arrives at an accurate result at a faster rate of convergence compared to the Runge-Kutta of order four (RK4), due to its stability and higher numerical order of convergence. This adaptation is essential for handling mathematical models with large number of non-linear dynamical equations. Therefore, the sixth order Runge-Kutta forward-backward sweep algorithm seeks to provide a more effective and efficient method due to its speed, accuracy, higher rate of convergence, suitability and versatility for real-time or practical applications such as the Epidemiological and general Biomedical models (see MATLAB code in Appendix).

REFERENCES

1. Adamu, S. (2023). Numerical solution of optimal control problems using block method. Electronic Journal of Mathematical Analysis and Applications, 11(2), 8. ISSN: 2090729X (online). Retrieved from http://ejmaa.journals.ekb.eg

2. Asamoah, J. K., Okyere, E., Abidemi A., Moore, S. E., Sun, G.,, Jin,, Z., Acheampong, E. and GordonOptimal, J. F. (2022), Control and comprehensive costeffectiveness analysis for COVID-19

3. Banu, M. S., Raju, I. and Mondal, S. (2021). A comparative study on classical fourth order and Butcher sixth order Runge-Kutta methods with initial and boundary value problems. International Journal of Material and Mathematical Sciences, 2(1), 8-21. https://doi.org/10.34104/ijmms.021.08021

4. Berkovitz, L. D. (1962). On control problems with bounded state variables. Journal of Mathematical Analysis and Applications, 5, 488-498. https://core.ac.uk/display/82704868

5. Guzman D´ıaz, D., Gomez-Aleixandre, J. and Coto, J. (2015). Direct backward/forward sweep algorithm for solving load power flows in AC droopregulated microgrids. IEEE Transactions on Power Systems, 30(6), 3151-3160. https://www.researchgate.net/publication/282530636

6. Kirk, D. E. (2004). Optimal control theory: An introduction . Dover Publications . 184-240. Retrieved from https://dokumen.tips/documents/optimal-control-theoryan-introduction.html?page=2

7. La Torre, D., Kunze, H., Ruiz-Galan, M., Malik, T. and Marsiglio, S. (2015). Optimal Control: Theory and Application to Science, Engineering, and Social Sciences. Abstract and Applied Analysis, 890527. https://doi.org/10.1155/2015/890527

8. Lenhart, S., & Workman, J. T. (2007). Optimal control applied to biological models (Chapman & Hall/CRC Mathematical and Computational Biology Series). Chapman and Hall/CRC. Retrieved from https://dokumen.pub/download/optimalcontrol-applied-to-biological-models-9781322628394-1322628394-978-1-4200-1141-8-

9. 1420011413 .html

10. Martcheva, M. (2015). An introduction to mathematical epidemiology (Texts in Applied Mathematics 61). Springer Science+Business Media New York, p. 237. https://doi.org/10.1007/978-1-4899-7612-3

11. Pontryagin,L. S., Boltyanskii, V. G., Gamkrelize, R. V. and Mishchenko, E. F. (1962). The Mathematical Theory of Optimal Processes. Wiley, New York.

12. Rose, G. R. (2015). Numerical Methods for Solving Optimal Control Problems. Master’s Thesis, University of Tennessee. Retrieved from https://trace.tennessee.edu/utk_gradthes/3401.